Astrophysical detections and databases for the mono deuterated species of acetaldehyde CH2DCOH and CH3COD

Laurent H. Coudert, L. Margules, C. Vastel, Roman A. Motiyenko, E. Caux, J. -C. Guillemin

A&A 624, A70 (2019)
https://doi.org/10.1051/0004-6361/201834827

Astronomy & Astrophysics

Astrophysical detections and databases for the mono deuterated species of acetaldehyde CH_2DCOH and CH_3COD★

L. H. Coudert[1], L. Margulès[2], C. Vastel[3], R. Motiyenko[2], E. Caux[3], and J.-C. Guillemin[4]

[1] Institut des Sciences Moléculaires d'Orsay, CNRS, Univ. Paris-Sud, Université Paris-Saclay, 91405 Orsay, France
e-mail: laurent.coudert@u-psud.fr
[2] Laboratoire de Physique des Lasers, Atomes et Molécules, UMR CNRS 8523, Bât. P5, Université de Lille I, 59655 Villeneuve d'Ascq Cedex, France
[3] IRAP, Université de Toulouse, CNRS, CNES, UPS, 9 Av. Colonel Roche, BP 44346, 31028 Toulouse Cedex 4, France
[4] Univ. Rennes, Ecole Nationale Superieure de Chimie de Rennes, CNRS, ISCR-UMR6226, 35000 Rennes, France

Received 11 December 2018 / Accepted 17 February 2019

ABSTRACT

Context. Detection of deuterated species may provide information on the evolving chemistry in the earliest phases of star-forming regions. For molecules with two isomeric forms of the same isotopic variant, gas-phase and solid-state formation pathways can be differentiated using their abundance ratio.
Aims. Spectroscopic databases for astrophysical purposes are built for the two mono deuterated isomeric species CH_2DCOH and CH_3COD of the complex organic molecule acetaldehyde. These databases can be used to search and detect these two species in astrophysical surveys, retrieving their column density and therefore abundances.
Methods. Submillimeter wave and terahertz transitions were measured for mono deuterated acetaldehyde CH_2DCOH which is a non-rigid species displaying internal rotation of its asymmetrical CH_2D methyl group. An analysis of a dataset consisting of previously measured microwave data and the newly measured transition was carried out with a model accounting for the large amplitude torsion.
Results. The frequencies of 2556 transitions are reproduced with a unitless standard deviation of 2.3 yielding various spectroscopic constants. Spectroscopic databases for astrophysical purposes were built for CH_2DCOH using the results of the present analysis and for CH_3COD using the results of a previous spectroscopic investigation. These two species were both searched for and are detected toward a low-mass star-forming region.
Conclusions. We report the first detection of CH_2DCOH (93 transitions) and the detection of CH_3COD (43 transitions) species in source B of the IRAS 16293−2422 young stellar binary system located in the ρ Ophiuchus cloud region, using the publicly available ALMA Protostellar Interferometric Line Survey.

Key words. astrochemistry – line: identification – ISM: molecules – ISM: abundances

1. Introduction

Acetaldehyde and its isotopic species have been the subject of many spectroscopic investigations, due to their astrophysical relevance and to the large amplitude nature of the internal rotation of the methyl group. The microwave spectrum of the normal species was first analyzed by Kilb et al. (1957) and has since then been investigated up to the ν_t = 4 torsional state (Herschbach 1959; Iijima & Tsuchiya 1972; Bauder & Günthard 1976; Kleiner et al. 1990, 1992, 1996; Smirnov et al. 2014), leading to its detection (Gilmore et al. 1976) in the interstellar medium (ISM). The isotopic species with a symmetrical CH_3 or CD_3 methyl group were also investigated (Kleiner et al. 1999; Coudert & López 2006; Elkeurti et al. 2010; Zaleski et al. 2017), but none are detected in the ISM. There is only a limited number of spectroscopic results for isotopic species with a partially deuterated CH_2D or CD_2H asymmetrical methyl group. The mono and bideuterated species CH_2DCOH and CD_2HCOH have been studied (Turner & Cox 1976; Turner et al. 1981), but only a few transitions characterized by a low K_a value were assigned as there was no model available at that time to treat the internal rotation of a partially deuterated methyl group.

Deuterated species are an important tool for understanding interstellar chemistry and specifically surface chemistry (Charnley et al. 1997; Ratajczak et al. 2011). Deuterium forms slightly stronger bonds than hydrogen at low temperatures (<100 K) and the abundance of deuterium-bearing molecules can become larger than the cosmic D/H ratio of 10^{-5}. A large fractionation ratio has been found in many environments such as dark clouds, low-mass and high-mass protostars, as well as protoplanetary disks (see Ceccarelli et al. 2014, for a review). For complex organic molecules (organic molecules containing at least six atoms, Herbst & van Dishoeck 2009), there usually exist two different isomeric mono deuterated species and their abundance ratio yields additional information about interstellar chemistry. This may allow differentiation of gas-phase and grain surface formation pathways. For example, the observed gas-phase $[CH_2DOH]/[CH_3OD]$ ratios found in the Orion KL compact ridge as well as the low-mass protostar IRAS 16293−2422, are found to scale inversely with $[HDO]/[H_2O]$ owing to the H/D exchange equilibrium between the hydroxyl (-OH) functional

★ Tables 3, 4, 7, and 8 are only available at the CDS via anonymous ftp to cdsarc.u-strasbg.fr (130.79.128.5) or via http://cdsarc.u-strasbg.fr/viz-bin/qcat?J/A+A/624/A70

groups of methanol and water in the ice (Faure et al. 2015). These observations are useful constraints for kinetics models of the deuterium chemistry occurring in the icy mantles of interstellar grains. This article focuses on the study of the mono deuterated CH_2DCOH and CH_3COD isotopic variants of acetaldehyde. We present in Sect. 2 the spectroscopic investigation of CH_2DCOH and the compilation of its database and that of CH_3COD. We first spectroscopically characterized the species that has a partially deuterated CH_2D methyl group, prior to designing its database. For the species with a symmetrical CH_3 methyl group, the database is based on the previous spectroscopic investigation by Elkeurti et al. (2010). We present in Sect. 3 the astrophysical search and detection of both species.

2. Spectroscopic investigation of CH_2DCOH

The main isotopic species of acetaldehyde and its isotopic variants with a symmetrical CH_3 or CD_3 methyl group were studied accounting for their internal rotation with theoretical approaches initially developed for methanol (Koehler & Dennison 1940; Burkhard & Dennison 1951; Ivash & Dennison 1953; Hecht & Dennison 1957a,b; Lees & Baker 1968; De Lucia et al. 1989). In the case of the present isotopic species, displaying internal rotation of an asymmetrical partially deuterated CH_2D methyl group, several theoretical models are also available and were applied to mono and bideuterated methyl formate and methanol (Margulès et al. 2009; Coudert et al. 2012, 2014; Pearson et al. 2012; Ndao et al. 2015).

In this section, the tunneling-rotation energy levels of CH_2DCOH are calculated using the approach developed for mono deuterated methyl formate (Margulès et al. 2009), based on the high-barrier internal axis method (IAM) approach of Hougen (1985) and Coudert & Hougen (1988). This IAM treatment is used to analyze the previously available microwave transitions (Turner & Cox 1976; Turner et al. 1981) and the submillimeter wave and terahertz transitions measured in this work.

2.1. Experimental

The transitions measured in this work were recorded in the 150–990 GHz frequency range using the Lille spectrometer (Zakharenko et al. 2015). The absorption cell was a stainless-steel tube (6 cm diameter, 220 cm long). The sample during measurements was at a pressure of about 10 Pa and at room temperature; the linewidth was limited by Doppler broadening. The frequency ranges 150–330, 400–660, and 780–990 GHz were covered with various active and passive frequency multipliers from VDI Inc. and an Agilent synthesizer (12.5–18.25 GHz) was used as the source of radiation. Estimated uncertainties for measured line frequencies are either 30 or 50 kHz depending on the observed signal-to-noise ratio (S/N) and the frequency range. Figure 1 shows two portions of the spectrum recorded in the submillimeter wave region.

2.2. Theory

The model developed previously for mono deuterated methyl formate (Margulès et al. 2009) can be applied to mono deuterated acetaldehyde CH_2DCOH with almost no changes. The coordinates used in this model are the usual Euler angles χ, θ, ϕ and a large amplitude angular coordinate, denoted α, parameterizing the internal rotation of the methyl group with respect to the

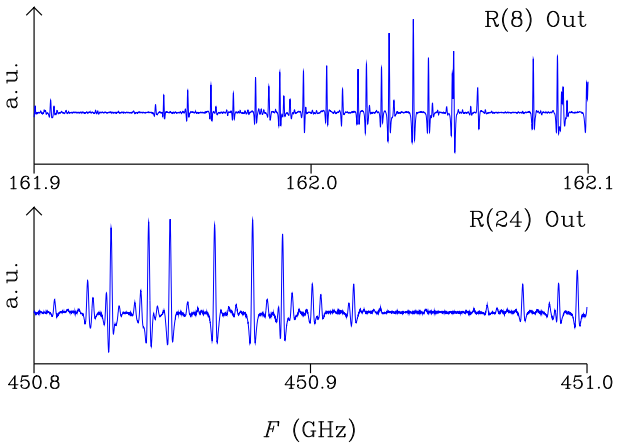

Fig. 1. Two portions of the spectrum recorded in the submillimeter wave region are plotted as a function of the frequency F in GHz. For the Out conformation, the *upper* and *lower panels* show tunneling components of the $R(8)$ and $R(24)$ transitions, respectively. The K-type structure can be clearly seen in both cases.

aldehyde group. Molecule-fixed coordinates of the atoms are obtained starting from the scheme introduced for the principal axis method in Sect. 3 of Hougen et al. (1994). The initial configuration drawn in their Fig. 1 defines atom positions in an $x'y'z'$ axis system such that the axis of internal rotation coincides with the z' axis. The methyl group atoms are numbered from 1 to 3, with atom 1 being the deuterium atom and atoms 2 and 3, the two hydrogen atoms. The large amplitude coordinate α is the dihedral angle ∠DCCO. Using Sect. 3.1 and Eqs. (1) and (2) of Margulès et al. (2009) allows us to retrieve atom positions in an xyz molecule-fixed axis system which, for any value of α, is the principal axis system in the I^r representation (Bunker 1979).

In agreement with the IAM approach of Hougen (1985) and Coudert & Hougen (1988), the non-superimposable equilibrium configurations of the molecule are chosen. There arise three energetically inequivalent configurations, shown in Fig. 2, identified by their configuration number n, with n = 1, 2, and 3, and characterized by $\alpha_{eq}^{(n)}$ the value of the torsional angle α around which the reference function is centered. Configurations 1 and 2 are the two C_1 symmetry Out configurations with the deuterium atom outside the $x'z'$ plane. They are higher in energy than Configuration 3, the C_s symmetry In configuration with the deuterium atom in the symmetry plane. The energy difference E_d between the zero point energy of the two Out configurations and that of the In configuration was estimated by Turner et al. (1981) to be 15.55 cm^{-1}.

Equations (12) and (13) of Margulès et al. (2009) should be used to obtain the tunneling matrix elements $H_{JK\gamma 1;JK'\gamma' 2}$ of the 1 → 2 tunneling path connecting the isoenergetic Configurations 1 and 2. Similarly, Eqs. (14) and (15) should be used for tunneling matrix elements $H_{JK\gamma 1;JK'\gamma' 3}$ of the 1 → 3 tunneling path connecting Configurations 1 and 3. In Eqs. (12)–(15) of Margulès et al. (2009), h_2 and h_3 are the magnitude of the tunneling splittings and θ_2, ϕ_2 and χ_3, θ_3, ϕ_3 are 5 Eulerian-type angles describing the rotational dependence of the tunneling matrix elements. In addition to these parameters, computing the rotation-torsion energy also requires the rotational constants of the In and Out conformations, A^{In}, B^{In}, C^{In} and A^{Out}, B^{Out}, C^{Out}, respectively, and their energy difference E_d.

When tunneling effects are small, the In conformation displays asymmetric-top rotational energies. For the + and −

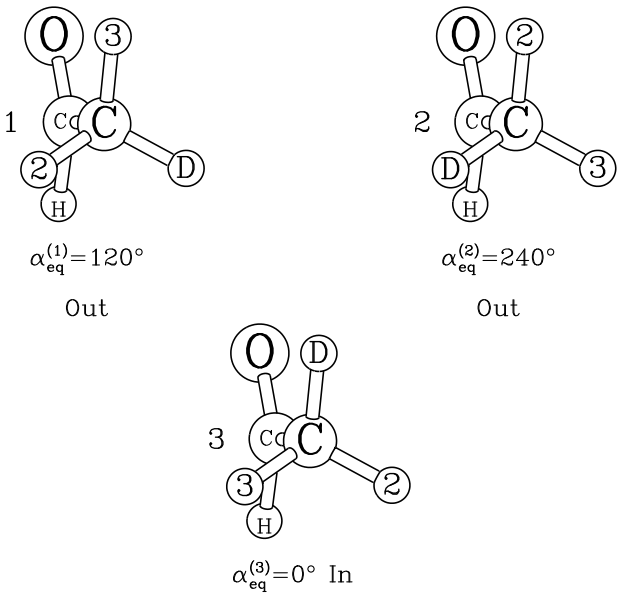

Fig. 2. Both energetically equivalent configurations of the Out conformation and the lower energy configuration of the In conformation are identified by their configuration number $n = 1, 2$, and 3. $\alpha_{eq}^{(n)}$ is the equilibrium value of the torsional angle $\alpha = \angle$DCCO. Configuration 3 displays a symmetry plane. Configurations 1 and 2 have C_1 symmetry.

sublevels arising from the Out conformation, Eq. (21) of Margulès et al. (2009) shows that $E_d \pm h_2$ should be added to the asymmetric-top rotational energies, where the upper (lower) sign is for the + (−) sublevel. As h_2 is negative (Hougen 1985; Coudert & Hougen 1988), the + sublevel is below the − sublevel. Parallel a-type and perpendicular b-type transitions arise within the In and Out conformations. For the latter conformation, the selection rule $\pm \leftrightarrow \pm$ holds. Perpendicular c-type transitions arise within the Out conformation only and obey the selection rule $\pm \leftrightarrow \mp$.

When tunneling effects are large, distortion terms to the tunneling matrix elements $H_{JK\gamma 1;JK'\gamma' 2}$ and $H_{JK\gamma 1;JK'\gamma' 3}$ should be added and those defined in Eq. (22) of Margulès et al. (2009) are used. Distortion effects to the five Eulerian-type angles are also accounted for using a polynomial-type expansion in $J(J+1)$.

Assigning the levels arising from numerical diagonalization of the Hamiltonian matrix in terms of rotational quantum numbers K_a and K_c and of + and − tunneling labels is not straightforward as the ordering of the tunneling sublevels changes for large enough K_a-values. The level assignment chosen here is consistent with symmetry and ensures a smooth variation of the tunneling splitting as a function of K_a for each J-value. For a given K_a-value, the tunneling matrix element $H_{JK\gamma 1;JK'\gamma' 2}$ couples the two members of an asymmetry doublet. A mixing of the $JK_a, K_c, \pm$ and $JK_a, K_c \pm 1, \mp$ rotational-tunneling sublevels arises and leads to forbidden transitions with even ΔK_a and ΔK_c (Turner et al. 1981). Such transitions were assigned in the previous investigations (Turner & Cox 1976; Turner et al. 1981) and in the present work.

The Eulerian-type angles θ_2, ϕ_2 and χ_3, θ_3, ϕ_3 were calculated numerically solving Eqs. (49) of Hougen (1985) for each tunneling motion and computing α-dependent atom positions with the structure of Kilb et al. (1957). Table 1 lists the computed values along with calculated rotational constants and dipole moment components. The latter were obtained from Turner & Cox (1978) using their favored orientation.

Table 1. Calculated molecular parameters.

Parameter	Value	Parameter	Value
χ_2	249.7	χ_3	244.4
θ_2	2.7	θ_3	4.2
ϕ_2	69.7	ϕ_3	66.5
A^{In}	1.618	A^{Out}	1.742
B^{In}	0.329	B^{Out}	0.314
C^{In}	0.288	C^{Out}	0.286
μ_x^{In}	1.164	μ_x^{Out}	1.054
μ_y^{In}	–	μ_y^{Out}	0.107
μ_z^{In}	2.491	μ_z^{Out}	2.538

Notes. Eulerian-type angles, in degrees, involved in the rotational dependence of the tunneling matrix elements, the rotational constants, in cm^{-1}, and the dipole moments components, in Debye, are listed for the In and Out conformations. For symmetry reason, the relation $\chi_2 = \phi_2 + \pi$ is fulfilled and μ_y^{In} is zero. Superscripted In and Out labels identify the rotational constants and dipole moment components.

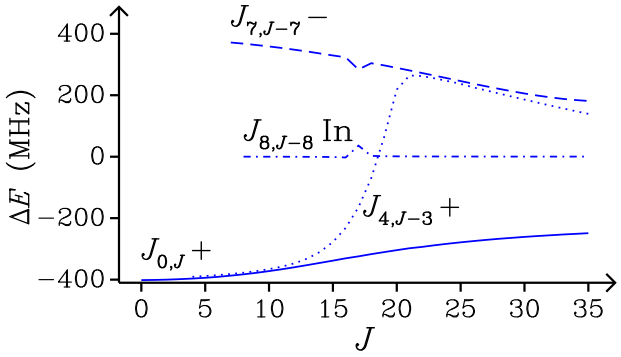

Fig. 3. Effects of the two tunneling motions ΔE are plotted in MHz as a function of J for several K_a-values and for all three tunneling sublevels. In identifies the level arising from the In conformation. + and − identify the tunneling sublevels arising from the Out conformation. The effects of the tunneling motion connecting the In and Out conformations can be seen for the $17_{8,9}$ In and $17_{7,10}$ − sublevels.

2.3. Line assignment and line frequency analysis

Starting from the results of Turner & Cox (1976), parallel a-type and perpendicular b-type transitions within the In conformation were assigned up to $J = 36$ and $K_a = 3$. This first set of transitions was fitted with a Watson-type Hamiltonian. Parallel a-type and perpendicular b- and c-type transitions within and between the + and − sublevels of the Out conformation were afterwards assigned up to $J = 36$ and $K_a = 4$, using the results of Turner et al. (1981). Fitting of this second set of transitions yielded rotational constants for the Out conformation, the magnitude of the tunneling splitting h_2, and the Eulerian-type angles θ_2 and ϕ_2. Both sets of transitions were then fitted together and the parameters corresponding to the $1 \rightarrow 3$ tunneling motion and the energy difference E_d could be obtained. Transitions perturbed by the coupling between the In and Out conformations (Cox et al. 2003) could then be included in the fit. New transitions were predicted and searched for. For the In conformation, it was possible to assign a-type transitions up to $J = 36$ and $K_a = 14$ and b-type transitions up to $J = 39$ and $K_a = 13$. For the Out conformation, a-type transitions were assigned up to $J = 35$ and $K_a = 14$ and perpendicular b- and c-type transition up to $J = 36$ and $K_a = 5$. The smaller number of perpendicular transitions assigned for the

Table 2. Assigned transitions.

	In		Out			
References	*a*-type	*b*-type	*a*-type	*b*-type	*c*-type	All
1	23	41	–	–	–	64
2	–	–	38	35	21	94
This work	488	502	1033	349	26	2398
All	511	543	1071	384	47	2556

Notes. The number of assigned *a*-, *b*-, and *c*-type transitions for each conformation in the two previous investigations (Turner & Cox 1976; Turner et al. 1981) and in this work. *c*-type transitions within the In conformation are not allowed. No transitions were assigned between the In and Out conformations.
Referances. (1) Turner & Cox (1976); (2) Turner et al. (1981).

Table 5. Spectroscopic parameters

Parameter	Value	Parameter	Value
$A^{\rm In}$	1.618 082 0(1)	$h_2 \times 10^3$	−13.399 9(7)
$B^{\rm In}$	0.329 050 33(1)	θ_2	2.094(7)
$C^{\rm In}$	0.288 103 10(1)	ϕ_2	69.717 8(7)
E_d	15.558 66(4)	$h_3 \times 10^3$	−7.72(7)
$A^{\rm Out}$	1.745 529(1)	χ_3	243.842(140)
$B^{\rm Out}$	0.313 917 38(1)	θ_3	3.992(11)
$C^{\rm Out}$	0.286 541 11(1)	ϕ_3	67.021(140)

Notes. Lowest order parameters obtained in the line position analysis of Sect. 2.3. Parameters are in $\rm cm^{-1}$ except for the angles θ_2, ϕ_2 and χ_3, θ_3, ϕ_3 which are in degrees. Uncertainties are given in parentheses in the same units as the last quoted digit.

Out conformation than for the In conformation may be due to two factors. The first possible explanation is decreased strength, due to a smaller value of the x dipole moment component of this conformation compared to that of the In conformation, as emphasized by Table 1. Alternatively, there may be a less favorable Boltzmann factor due to a larger A rotational constant for the Out conformation than for the In conformation and the fact that the Out conformation is 15 $\rm cm^{-1}$ above the In conformation. Table 2 lists the number of assigned transitions for each conformation counting forbidden even ΔK_a and ΔK_c transitions of the Out conformation as *a*-type transitions.

In the final analysis, experimental frequencies were introduced in a least-squares fit procedure where they were given a weight equal to the inverse of their experimental uncertainty squared. Unresolved K-type doublets were treated as in Margulès et al. (2009). The rotational Watson-type Hamiltonians used for the In and Out conformations were written using Watson's A-set of distortion parameters (Watson 1967, 1968a,b). The root mean square value of the observed minus calculated frequency is 0.054 MHz for transitions within the In conformation, 0.193 MHz for transitions within the Out conformation, and 0.151 MHz for all transitions. The unitless standard deviation of this final analysis is 2.3 For the whole dataset, assignments, observed and calculated frequencies, and residuals are listed in Table 3 available at the CDS. This table displays 13 columns. Columns 1–4 (5–8) give the assignment of the upper (lower) level in terms of J, K_a, K_c rotational quantum numbers and a vibrational label v. The latter is zero for the In conformation and + or − for the two tunneling sublevels of the Out conformation (see Sect. 2.2). Column 9 is the observed frequency in MHz; Col. 10 its uncertainty in kHz; Col. 11 is the observed minus calculated residual in kHz; Col. 12 is blank for a single line and d for a line belonging to an unresolved K-type doublet; and Col. 13 gives the reference from which the transition was taken. Table 4, also available at the CDS, lists the parameters determined in the analysis. This table displays 3 columns. Column 1 gives the parameter name; Col. 2 its value; and Col. 3 its uncertainty. Table 5 only lists the lowest order parameters. For the rotational constants, the calculated values in Table 1 are within 0.01 $\rm cm^{-1}$ from the experimental values in Table 5. For the Eulerian-type angles describing the rotational dependence of the tunneling matrix elements, the discrepancies are at most 5%.

Table 6. Partition function $Q_{\rm rot}$ of CH_2DCOH and CH_3COD.

	$Q_{\rm rot}$	
T/K	CH_2DCOH	CH_3COD
2.725	12.4	25.0
5.000	30.8	61.0
9.375	90.3	154.9
18.75	343.0	435.7
37.50	1269.7	1234.9
75.00	4530.7	3740.2
150.0	16806.8	13769.4
225.0	36862.3	33051.9
300.0	64872.9	63715.8

Notes. Partition functions are given for each temperature T in Kelvin.

2.4. Spectroscopic database for CH_2DCOH and CH_3COD

For CH_2DCOH, the spectroscopic database was built using the results of the previous sections. Transitions were calculated up to $J = 26$ and their line strength and line intensity were computed using the dipole moment components in Table 1. For CH_3COD, the results of the analysis carried out by Elkeurti et al. (2010) were used and transitions were calculated using the same maximum value of J. Partition functions $Q_{\rm rot}$, listed in Table 6, were computed for several temperatures taking a degeneracy factors equal to $(2J + 1)$. A zero energy was taken for the In conformation 0_{00} level of CH_2DCOH and for the $\nu_t = 0$ A_1 symmetry 0_{00} level of CH_3COD. For both species, lines were selected using the procedure in the JPL database catalog line files (Pickett et al. 1998). An intensity cutoff that depended on the line frequency was taken. Its value in $\rm nm^2 \cdot MHz$ units at 300 K is

$$10^{\rm LOGSTR0} + (F/300\,000)^2 \times 10^{\rm LOGSTR1}, \quad (1)$$

where F is the frequency in MHz, and LOGSTR0 and LOGSTR1 are two dimensionless constants both set to −8. The linelists, given in Table 7 for CH_2DCOH and in Table 8 for CH_3COD, are available at the CDS. They are formatted in the same way as the catalog line files of the JPL database (Pickett et al. 1998) and display 16 columns. Columns 1–3 contain respectively the line frequency (FREQ) in MHz, the error (ERR) in MHz, and the base 10 logarithm of the line intensity (LGINT) in $\rm nm^2 \cdot MHz$ units at 300 K. Columns 4–6 give the degrees of freedom of the rotational partition function (DR), the lower state energy (ELO) in $\rm cm^{-1}$, and the upper state degeneracy (GUP), respectively. Columns 7 and 8 contain the species tag (TAG) and format number (QNFMT), respectively. Finally, cols. 9–12 (13–16) give the assignment of the upper (lower) level in terms of J, K_a, K_c, and a vibrational quantum number. For CH_2DCOH, this quantum number is zero for the levels of the In conformation and 1 or 2 for the + and − sublevels of the

Out conformation. For CH_3COD, this label is 0 for A-symmetry levels and 1 and 2 for E-symmetry levels when $\nu_t = 0$. This label is 3 and 4 for E-symmetry levels and 5 for A-symmetry levels when $\nu_t = 1$. For both species, a minimum value of 10 kHz was selected for the calculated error (ERR). For observed unblended microwave lines, the line frequency (FREQ) and the error (ERR) were replaced by their experimental values. This is then indicated by a negative species tag.

3. Astrophysical observations

High deuterium fractionation has been observed in various types of environments such as prestellar cores, hot cores, and hot corinos. Its study is considered to be an efficient probe for studying the physical and chemical conditions of these environments and help us to understand their formation. This is especially interesting for the so-called complex organic molecules such as methanol and bigger molecules for which it may allow differentiation of gas-phase and solid-state formation pathways.

We first used the ASAI (Astrochemical Surveys At Iram)[1] IRAM-30 m Large Program data to search for CH_2DCOH and CH_3COD. The goal of these observations was to carry out unbiased millimeter line surveys between 80 and 272 GHz of a sample of ten template sources, which fully cover the first stages of the formation process of solar-type stars, from prestellar cores to the late protostellar phase (Lefloch et al. 2018). We used the CASSIS[2] software for the line identification in the publicly available ASAI data[3]. We conclude that these species are not detected in all ASAI sources with the single-dish observations, either because they are only present in the dense and hot regions as the hot corinos, or present with a too small abundance in the colder extended envelope to be detected by these observations.

We then used ALMA interferometric observations toward the very line rich source IRAS 16293−2422 (hereafter IRAS16293). IRAS16293 is a deeply embedded young stellar binary system located in the L1689 region in the ρ Ophiuchus cloud region, extensively studied through millimeter and submillimeter single-dish and interferometer observations. It has a cold outer envelope (with spatial scales of up to ∼6000 au) (Jaber Al-Edhari et al. 2017) and a hot corino at scales of ∼100 au (Jørgensen et al. 2016). Due to its hot-core-like properties, a wealth of complex organic have been reported toward its two binary components: I16293A and I16293B, separated by 5″ (Wootten 1989). We used the publicly available ALMA Protostellar Interferometric Line Survey (PILS, Jørgensen et al. 2016), an unbiased spectral survey of IRAS16293 covering a frequency range of about [329–363] GHz of ALMA's Band 7, performed in ALMA's Cycle 2 (project-id: 2013.1.00278.S). Full observational details are given in Jørgensen et al. 2016. The entire raw dataset of this survey is accessible on the ALMA website. In this work, we only used the data obtained with the 12 m dishes array (∼38 antennas in the array at the time of observations), that we reprocessed using the standard pipeline scripts to obtain data-cubes with the ultimate spectral resolution of $\delta v \sim 0.25$ km s^{-1}, in a 0.5″ beam located ∼1″ east of source B (α_{J2000} = 16 h 32 m 22.5375 s; δ_{J2000} = −24° 28′ 32.555″), necessary to decrease the damaging effect of line blending.

We first computed local thermodynamic equilibrium (LTE) synthetic spectra, using the CASSIS software, of the expected brightest lines of CH_2DCOH and CH_3COD species in the PILS frequency range, limiting the search for transitions with $A_{i,j} \geq 0.001$ s^{-1} and $E_{up} \leq 500$ K. For the synthetic spectra we assumed a source size larger than the beam (3″), an excitation temperature of 100 K, a line width of 0.8 km s^{-1}, and a column density of 5×10^{14} cm^{-2} for CH_2DCOH and 3.5×10^{14} cm^{-2} for CH_3COD respectively. We limited the search in a 10 GHz spectral band among the 34 GHz of the PILS survey, where the density of CH_2DCOH and CH_3COD lines was the largest. The goal being the identification of the CH_2DCOH and CH_3COD lines, we did not optimize neither the data processing, nor the CASSIS LTE modeling to reproduce the line intensities. Figures A.1 and A.2 show the detection of 93 CH_2DCOH lines and 43 CH_3COD lines in this 10 GHz frequency range (among, respectively, the 101 and 99 present in the frequency range with the thresholds used). Tables A.1 and A.2 show the detected lines parameters. Note that Jørgensen et al. (2018) reported the detection of CH_3COD in IRAS 16293-2422B.

It can be noted that with the thresholds used, all CH_2DCOH lines are detected, except transition $18_{3,16,0}$–$17_{3,15,0}$, which is predicted to be much brighter than observed and transitions $20_{11,10,1}$–$19_{11,9,1}$, $20_{11,9,1}$–$19_{11,8,1}$, $20_{11,9,2}$–$19_{11,8,2}$, and $20_{11,10,2}$–$19_{11,9,2}$, which have an $E_{up} \geq 450$ K. For CH_3COD, all undetected transitions but two have an $E_{up} \geq 340$ K. The non-detection of some lines is therefore only due to the sensitivity limit of the PILS survey.

4. Conclusions

The rotation-torsion spectrum of the non-rigid mono deuterated acetaldehyde CH_2DCOH was experimentally and theoretically investigated. Due to the internal rotation of the asymmetrical CH_2D methyl group, the ground vibrational state of the molecule is split into three torsional sublevels. Transitions within and between these sublevels were measured in the submillimeter wave and terahertz spectra described in Sect. 2.1. These transitions along with previously measured ones (Turner & Cox 1976; Turner et al. 1981) were fitted using the IAM treatment (Hougen 1985; Coudert & Hougen 1988) presented in Sect. 2.2. The frequency of 2556 transitions could be reproduced with a 2.3 unitless standard deviation. The good agreement between calculated spectroscopic parameters in Table 1 and their experimental values in Table 5 emphasizes a fairly good understanding of the three first torsional levels of mono deuterated acetaldehyde CH_2DCOH.

The present analysis allowed us to evidence two types of tunneling motions. In addition to the tunneling motion connecting the two energetically equivalent Out configurations, dealt with in mono deuterated methyl formate (Margulès et al. 2009), it was possible to observe the tunneling motion connecting the energetically inequivalent In and Out conformations. This second tunneling motion leads only to shifts as it connects levels that already have different energies (Cox et al. 2003). Figure 3 illustrates the effects of both tunneling motions. The tunneling motion connecting the two energetically equivalent Out configurations leads to an 800 MHz tunneling splitting clearly visible in this figure. The effects of the tunneling motion connecting the In and Out conformations are smaller and become important when level crossings occur.

The results of the analysis were used to build a database for astrophysical purposes for CH_2DCOH. A similar database, for the isomeric mono deuterated species CH_3COD, was compiled starting from the results of the previously published analysis of Elkeurti et al. (2010). With these databases, we have conducted a search of CH_2DCOH and CH_3COD lines in the publicly

[1] http://www.oan.es/asai/
[2] http://cassis.irap.omp.eu/
[3] http://www.iram.fr/ILPA/LP007/

available ASAI IRAM-30m Large Program and the ALMA Protostellar Interferometric Line Survey (PILS, Jørgensen et al. 2016). Both CH_2DCOH (93 transitions) and CH_3COD (43 transitions) species were detected in the IRAS 16293-2422 source B young stellar object alone, located in the ρ Ophiuchus cloud region. Tables A.1 and A.2 list the transitions identified in this source.

References

Bauder, A., & Günthard, H. H. 1976, J. Mol. Spectr., 60, 290
Bunker, P. R. 1979, Molecular Symmetry and Spectroscopy, 1st edn. (New York: Academic Press)
Burkhard, D. G., & Dennison, D. M. 1951, Phys. Rev., 84, 408
Ceccarelli, C., Caselli, P., Bockelée-Morvan, D., et al. 2014, Protostars and Planets VI, 859
Charnley, S. B., Tielens, A. G. G. M., & Rodgers, S. D. 1997, ApJ, 482, L203
Coudert, L. H., & Hougen, J. T. 1988, J. Mol. Spectr., 130, 86
Coudert, L. H., & López, J. C. 2006, J. Mol. Spectr., 239, 135
Coudert, L. H., Margulès, L., Huet, T. R., et al. 2012, A&A, 543, A46
Coudert, L. H., Zemouli, M., Motiyenko, R. A., Margulès, L., & Klee, S. 2014, J. Chem. Phys., 140, 064307
Cox, A. P., Hughes, K. H., & MacDonald, J. N. 2003, Mol. Phys., 101, 569
De Lucia, F. C., Herbst, E., Anderson, T., & Helminger, P. 1989, J. Mol. Spectr., 134, 395
Elkeurti, M., Coudert, L. H., Medvedev, I. R., et al. 2010, J. Mol. Spectr., 263, 145
Faure, A., Faure, M., Theulé, P., Quirico, E., & Schmitt, B. 2015, A&A, 584, A98
Gilmore, W., Morris, M., Johnson, D. R., et al. 1976, ApJ, 204, 43
Hecht, K. T., & Dennison, D. M. 1957a, J. Chem. Phys., 26, 31
Hecht, K. T., & Dennison, D. M. 1957b, J. Chem. Phys., 26, 48
Herbst, E., & van Dishoeck, E. F. 2009, ARA&A, 47, 427
Herschbach, D. R. 1959, J. Chem. Phys., 31, 91
Hougen, J. T. 1985, J. Mol. Spectr., 114, 395
Hougen, J. T., Kleiner, I., & Godefroid, M. 1994, J. Mol. Spectr., 163, 559
Iijima, T., & Tsuchiya, S. 1972, J. Mol. Spectr., 44, 88
Ivash, E. V., & Dennison, D. M. 1953, J. Chem. Phys., 21, 1804
Jaber Al-Edhari, A., Ceccarelli, C., Kahane, C., Viti, S., et al. 2017, A&A, 597, 40
Jørgensen, J. K., van der Wiel, M. H. D., Coutens, A., et al. 2016, A&A, 595, A117
Jørgensen, J. K., Müller, H. S. P., Calcutt, H., et al. 2018, A&A, 620, A170
Kilb, R. W., Lin, C. C., & Wilson, Jr., E. B. 1957, J. Chem. Phys., 26, 1695
Kleiner, I., Godefroid, M., Herman, M., & McKellar, A. R. W. 1990, J. Mol. Spectr., 142, 238
Kleiner, I., Hougen, J. T., Suenram, R. D., Lovas, F. J., & Godefroid, M. 1992, J. Mol. Spectr., 153, 578
Kleiner, I., Hougen, J. T., Grabow, J.-U., et al. 1996, J. Mol. Spectr., 179, 41
Kleiner, I., Lopez, J. C., Blanco, S., McKellar, A. R. W., & Moazzen-Ahmadi, N. 1999, J. Mol. Spectr., 197, 275
Koehler, J. S., & Dennison, D. M. 1940, Phys. Rev., 57, 1006
Lees, R. M., & Baker, J. G. 1968, J. Chem. Phys., 48, 5299
Lefloch, B., Bachiller, R., Ceccarelli, C., et al. 2018, MNRAS, 477, 4792
Margulès, L., Coudert, L. H., Møllendal, H., et al. 2009, J. Mol. Spectr., 254, 55
Ndao, M., Kwabia Tchana, F., Coudert, L. H., et al. 2015, J. Mol. Spectr., 326, 136
Pearson, J. C., Yu, S., & Drouin, B. J. 2012, J. Mol. Spectr., 280, 119
Pickett, H. M., Poynter, R. L., Cohen, E. A., et al. 1998, J. Quant. Spectr. Radiat. Transfer, 60, 883
Ratajczak, A., Taquet, V., Kahane, C., et al. 2011, A&A, 528, L13
Smirnov, I. A., Alekseev, E. A., Ilyushin, V. V., et al. 2014, J. Mol. Spectr., 295, 44
Turner, P. H., & Cox, A. P. 1976, Chem. Phys. Lett., 42, 84
Turner, P. H., & Cox, A. P. 1978, J. Chem. Soc. Faraday Trans., 2, 533
Turner, P. H., Cox, A. P., & Hardy, J. A. 1981, J. Chem. Soc. Faraday Trans., 2, 1217
Watson, J. K. G. 1967, J. Chem. Phys., 46, 1935
Watson, J. K. G. 1968a, J. Chem. Phys., 48, 181
Watson, J. K. G. 1968b, J. Chem. Phys., 48, 4517
Wootten, A. 1989, ApJ, 337, 858
Zakharenko, O., Motiyenko, R. A., Margulès, L., & Huet, T. R. 2015, J. Mol. Spectr., 317, 41
Zaleski, D. P., Duan, C., Carvajal, M., Kleiner, I., & Prozument, K. 2017, J. Mol. Spectr., 342, 17

Appendix A: Additional material

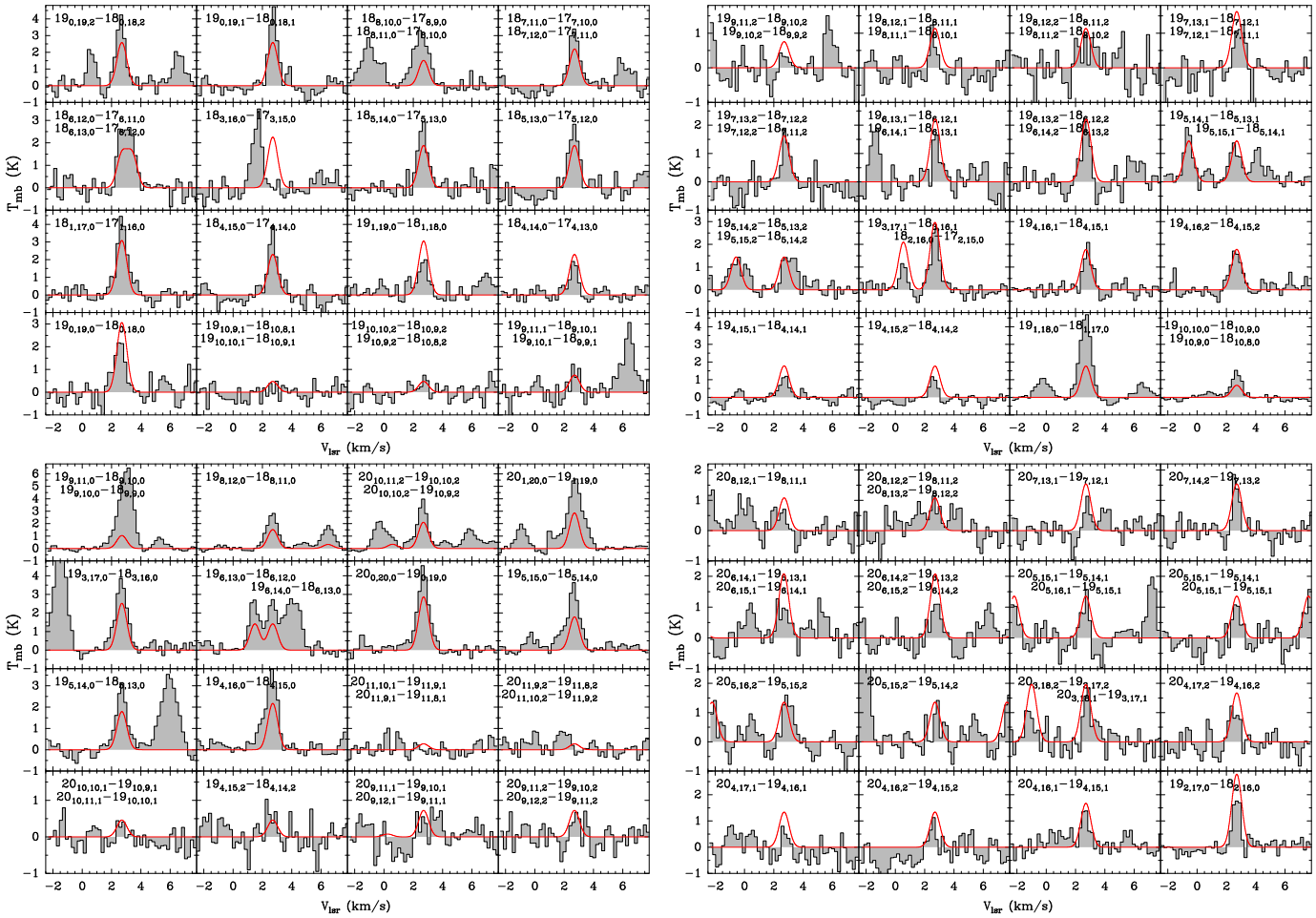

Fig. A.1. CH_2DCOH observed (in black) and modeled (in red) lines. The lines have been shifted at a V_{LSR} of 2.7 km s^{-1}. The quantum numbers are indicated with a sorting in frequency, for $A_{i,j} \geq 0.001$ s^{-1} and $E_{up} \leq 500$ K. In the case of multiple transitions, the quantum numbers are indicated from the *left* to the *right*, with increasing V_{LSR}. CH_2DCOH ($18_{3,16,0} - 17_{3,15,0}$) is not detected, or predicted to be too bright, and the nearby line is $HCOOCH_3$.

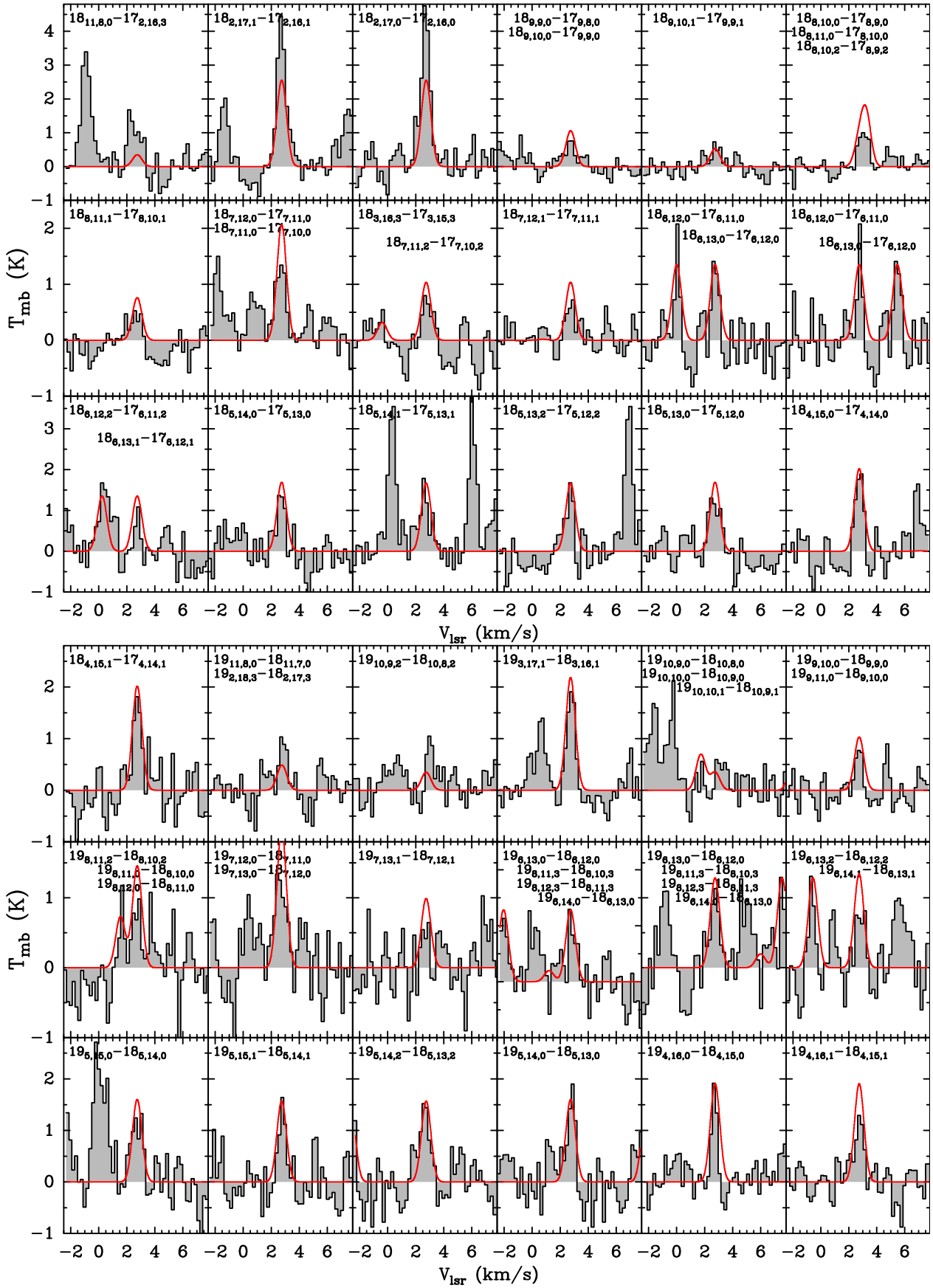

Fig. A.2. CH_3COD observed (in black) and modeled (in red) lines. The lines have been shifted at a V_{LSR} of 2.7 km s^{-1}. The quantum numbers are indicated with a sorting in frequency, for $A_{i,j} \geq 0.001$ s^{-1} and $E_{up} \leq 500$ K. In the case of multiple transitions, the quantum numbers are indicated from the left to the right, with increasing V_{LSR}.

Table A.1. CH_2DCOH transitions in the frequency range considered and their main parameters.

Transition	Frequency (MHz)	E_{up} (K)	A_{ij} $10^{-3}(s^{-1})$	τ_{peak} 10^{-2}	$\int T_{mb}dv$ (K km s^{-1})	Blend
$19_{0,19,2}$–$18_{0,18,2}$	332931.260	183.86	1.34	2.1	3.17	
$19_{0,19,1}$–$18_{0,18,1}$	332944.584	183.83	1.34	2.1	3.23	
$18_{8,10,0}$–$17_{8,9,0}$	333350.436	272.44	1.00	0.44	4.24*	Unidentified
$18_{8,11,0}$–$17_{8,10,0}$	333350.436	272.44	1.00	0.44	4.24*	Unidentified
$18_{7,12,0}$–$17_{7,11,0}$	333516.699	244.24	1.11	0.714	2.94	
$18_{7,11,0}$–$17_{7,10,0}$	333516.714	244.24	1.11	0.714	2.94	
$18_{6,13,0}$–$17_{6,12,0}$	333732.064	219.82	1.16	1.04	1.64	
$18_{6,12,0}$–$17_{6,11,0}$	333732.844	219.82	1.16	1.04	1.64	
$18_{3,16,0}$–$17_{3,15,0}$	333839.703	169.17	1.07	1.58	ND	
$18_{5,14,0}$–$17_{5,13,0}$	334088.542	199.20	1.21	1.44	2.35	
$18_{5,13,0}$–$17_{5,12,0}$	334115.850	199.20	1.21	1.25	2.34	
$18_{1,17,0}$–$17_{1,16,0}$	334365.794	156.58	1.30	2.78	3.81	
$18_{4,15,0}$–$17_{4,14,0}$	334557.044	182.39	1.25	1.57	2.59	
$19_{1,19,0}$–$18_{1,18,0}$	334809.383	163.53	1.32	2.68	1.88	
$18_{4,14,0}$–$17_{4,13,0}$	335113.524	182.46	1.26	1.57	1.20	
$19_{0,19,0}$–$18_{0,18,0}$	335405.895	163.43	1.32	2.17	2.18	
$19_{10,10,1}$–$18_{10,9,1}$	341877.416	394.14	1.06	0.088	0.13	
$19_{10,9,1}$–$18_{10,8,1}$	341877.416	394.14	1.06	0.088	0.13	
$19_{10,10,2}$–$18_{10,9,2}$	341892.791	394.12	1.06	0.088	0.32	
$19_{10,9,2}$–$18_{10,8,2}$	341892.791	394.12	1.06	0.088	0.32	
$19_{9,10,1}$–$18_{9,9,1}$	341931.674	354.75	1.13	0.162	0.70	
$19_{9,11,1}$–$18_{9,10,1}$	341931.674	354.75	1.13	0.162	0.70	
$19_{9,10,2}$–$18_{9,9,2,}$	341947.390	354.73	1.13	0.162	0.25	
$19_{9,11,2}$–$18_{9,10,2}$	341947.390	354.73	1.13	0.162	0.25	
$19_{8,11,1}$–$18_{8,10,1}$	341995.513	319.49	1.20	0.278	0.49	
$19_{8,12,1}$–$18_{8,11,1}$	341995.513	319.49	1.20	0.278	0.49	
$19_{8,12,2}$–$18_{8,11,2}$	342011.315	319.47	1.20	0.278	1.18	
$19_{8,11,2}$–$18_{8,10,2}$	342011.315	319.47	1.20	0.278	1.18	
$19_{7,12,1}$–$18_{7,11,1}$	342077.981	288.38	1.26	0.447	1.05	
$19_{7,13,1}$–$18_{7,12,1}$	342077.982	288.38	1.26	0.447	1.05	
$19_{7,12,2}$–$18_{7,11,2}$	342093.640	288.35	1.26	0.448	1.18	
$19_{7,13,2}$–$18_{7,12,2}$	342093.641	288.35	1.26	0.448	1.18	
$19_{6,14,1}$–$18_{6,13,1}$	342193.339	261.41	1.30	0.675	0.93	
$19_{6,13,1}$–$18_{6,12,1}$	342193.369	261.41	1.30	0.675	0.93	
$19_{6,14,2}$–$18_{6,13,2}$	342213.598	261.38	1.30	0.675	1.44	
$19_{6,13,2}$–$18_{6,12,2}$	342213.629	261.38	1.32	0.675	1.44	
$19_{5,15,1}$–$18_{5,14,1}$	342377.347	238.61	1.36	0.954	1.25	
$19_{5,14,1}$–$18_{5,13,1}$	342381.081	238.61	1.36	0.954	1.26	
$19_{5,15,2}$–$18_{5,14,2}$	342394.785	238.58	1.36	0.955	0.97*	$HCOOCH_3$
$19_{5,14,2}$–$18_{5,13,2}$	342398.534	238.58	1.36	0.955	1.42	
$18_{2,16,0}$–$17_{2,15,0}$	342601.088	162.68	1.40	2.62	1.93	
$19_{3,17,1}$–$18_{3,16,1}$	342603.552	205.47	1.43	1.57	0.76	
$19_{3,17,2}$–$18_{3,16,2}$	342607.900	205.45	1.43	1.58	?*	CH_3OCH_3 and CH_3COD
$19_{4,16,1}$–$18_{4,15,1}$	342669.740	219.98	1.39	1.26	1.39	
$19_{4,16,2}$–$18_{4,15,2}$	342683.025	219.96	1.40	1.27	1.65	
$19_{4,15,1}$–$18_{4,14,1}$	342791.348	220.00	1.41	1.14	0.93	
$19_{4,15,2}$–$18_{4,14,2}$	342805.115	219.97	1.40	1.26	0.69	
$19_{1,18,0}$–$18_{1,17,0}$	351688.961	173.46	1.52	2.46	4.48	
$19_{11,8,0}$–$18_{11,7,0}$	351692.369	396.45	1.02	0.078	1.03*	$HCOOCH_3$
$19_{11,9,0}$–$18_{11,8,0}$	351692.369	396.45	1.02	0.078	1.03*	$HCOOCH_3$
$19_{10,10,0}$–$18_{10,9,0}$	351747.890	356.99	1.11	0.145	1.27	
$19_{10,9,0}$–$18_{10,8,0}$	351747.890	356.99	1.11	0.145	1.27	
$19_{9,10,0}$–$18_{9,9,0}$	351823.926	321.28	1.19	0.254	?*	$HCOOCH_3$
$19_{9,11,0}$–$18_{9,10,0}$	351823.926	321.28	1.19	0.254	?*	$HCOOCH_3$

Notes. Integrated intensities noted with a * are certainly blended with lines from other species, indicated in Col. 7 when identified.

Table A.1. continued.

Transition	Frequency (MHz)	E_{up} (K)	A_{ij} $10^{-3}(s^{-1})$	τ_{peak} 10^{-2}	$\int T_{mb}dv$ (K km s^{-1})	Blend
$19_{8,11,0}$–$18_{8,10,0}$	351931.099	289.33	1.26	0.418	2.70	
$19_{8,12,0}$–$18_{8,11,0}$	351931.100	289.33	1.26	0.418	2.70	
$19_{7,13,0}$–$18_{7,12,0}$	352089.199	261.14	1.33	0.646	3.40	
$19_{7,12,0}$–$18_{7,11,0}$	352089.229	261.14	1.33	0.646	3.40	
$20_{1,20,0}$–$19_{1,19,0}$	352116.723	180.43	1.53	2.37	6.58	
$19_{3,17,0}$–$18_{3,16,0}$	352277.871	186.08	1.50	1.72	3.79	
$19_{6,14,0}$–$18_{6,13,0}$	352345.833	236.73	1.39	0.942	2.57	
$19_{6,13,0}$–$18_{6,12,0}$	352347.267	236.73	1.39	0.942	2.16	
$20_{0,20,0}$–$19_{0,19,0}$	352582.537	180.36	1.54	1.98	4.23	
$19_{5,15,0}$–$18_{5,14,0}$	352761.312	216.13	1.44	1.29	2.84	
$19_{5,14,0}$–$18_{5,13,0}$	352805.826	216.13	1.44	1.16	2.71	
$19_{4,16,0}$–$18_{4,15,0}$	353255.649	199.34	1.48	1.67	3.22	
$20_{11,10,1}$–$19_{11,9,1}$	359806.816	454.93	1.19	0.041	ND	
$20_{11,9,1}$–$19_{11,8,1}$	359806.816	454.93	1.19	0.041	ND	
$20_{11,10,2}$–$19_{11,9,2}$	359822.499	454.91	1.19	0.041	ND	
$20_{11,9,2}$–$19_{11,8,2}$	359822.499	454.91	1.19	0.041	ND	
$20_{10,10,1}$–$19_{10,9,1}$	359862.321	411.42	1.28	0.08	0.15	
$20_{10,11,1}$–$19_{10,10,1}$	359862.321	411.42	1.28	0.08	0.15	
$20_{10,11,2}$–$19_{10,10,2}$	359878.052	411.39	1.28	0.08	0.58	
$20_{10,10,2}$–$19_{10,9,2}$	359878.052	411.39	1.28	0.08	0.58	
$20_{9,11,1}$–$19_{9,10,1}$	359923.175	372.03	1.36	0.146	0.33	
$20_{9,12,1}$–$19_{9,11,1}$	359923.175	372.03	1.36	0.146	0.33	
$20_{9,12,2}$–$19_{9,11,2}$	359939.252	372.00	1.36	0.146	0.39	
$20_{9,11,2}$–$19_{9,10,2}$	359939.252	372.00	1.36	0.146	0.39	
$20_{8,13,1}$–$19_{8,12,1}$	359995.506	336.77	1.43	0.25	0.36	
$20_{8,12,1}$–$19_{8,11,1}$	359995.506	336.77	1.43	0.25	0.36	
$20_{8,12,2}$–$19_{8,11,2}$	360011.751	336.74	1.43	0.25	0.97	
$20_{8,13,2}$–$19_{8,12,2}$	360011.751	336.74	1.43	0.25	0.97	
$20_{7,14,1}$–$19_{7,13,1}$	360089.336	305.66	1.50	0.4	0.49	
$20_{7,13,1}$–$19_{7,12,1}$	360089.337	305.66	1.50	0.4	0.49	
$20_{7,14,2}$–$19_{7,13,2}$	360105.836	305.63	1.50	0.4	0.93	
$20_{7,13,2}$–$19_{7,12,2}$	360105.837	305.63	1.50	0.4	0.93	
$20_{6,15,1}$–$19_{6,14,1}$	360222.466	278.70	1.56	0.6	0.71	
$20_{6,14,1}$–$19_{6,13,1}$	360222.514	278.70	1.56	0.6	0.71	
$20_{6,15,2}$–$19_{6,14,2}$	360229.586	278.67	1.55	0.598	0.86	
$20_{6,14,2}$–$19_{6,13,2}$	360229.635	278.67	1.55	0.598	0.86	
$20_{5,16,1}$–$19_{5,15,1}$	360436.463	255.90	1.61	0.845	0.75	
$20_{5,15,1}$–$19_{5,14,1}$	360442.349	255.91	1.61	0.845	0.68	
$20_{5,16,2}$–$19_{5,15,2}$	360454.387	255.88	1.61	0.846	1.33	
$20_{5,15,2}$–$19_{5,14,2}$	360460.297	255.88	1.61	0.846	0.71	
$20_{3,18,1}$–$19_{3,17,1}$	360604.606	222.77	1.68	1.39	1.10	
$20_{3,18,2}$–$19_{3,17,2}$	360609.057	222.76	1.68	1.39	0.72	
$20_{4,17,2}$–$19_{4,16,2}$	360775.557	237.27	1.65	1.05	0.90	
$20_{4,17,1}$–$19_{4,16,1}$	360793.435	237.30	1.32	0.894	0.31	
$20_{4,16,2}$–$19_{4,15,2}$	360921.148	237.29	1.32	0.837	0.45	
$20_{4,16,1}$–$19_{4,15,1}$	360938.372	237.32	1.65	1.12	0.97	
$19_{2,17,0}$–$18_{2,16,0}$	361419.301	180.02	1.64	1.93	1.25	

Table A.2. CH_3COD transitions in the frequency range considered and their main parameters.

Transition	Frequency (MHz)	E_{up} (K)	A_{ij} $10^{-3}(s^{-1})$	τ_{peak} 10^{-2}	$\int T_{mb}dv$ (K km s^{-1})	Blend
$18_{11,8,0}$–$17_{2,16,3}$	333512.727	361.37	1.31	0.1916	1.05*	Unidentified
$18_{2,17,1}$–$17_{2,16,1}$	333618.976	160.35	1.31	1.2480	3.46	
$18_{2,17,0}$–$17_{2,16,0}$	333645.049	160.33	1.31	1.2470	3.66	
$18_{11,8,1}$–$17_{11,7,1}$	334527.523	360.87	1.31	0.1909	ND	
$18_{9,9,2}$–$17_{9,8,2}$	340477.155	293.37	1.06	0.2805	ND	
$18_{9,10,0}$–$17_{9,9,0}$	340497.126	293.33	1.06	0.2806	0.54	
$18_{9,9,0}$–$17_{9,8,0}$	340497.126	293.33	1.06	0.2806	0.54	
$18_{9,10,1}$–$17_{99,1}$	340515.997	293.32	1.06	0.2806	0.48	
$18_{8,11,0}$–$17_{8,10,0}$	340625.911	264.41	1.13	0.3935	0.95	
$18_{8,10,0}$–$17_{8,9,0}$	340625.911	264.41	1.13	0.3935	0.95	
$18_{8,10,2}$–$17_{8,9,2}$	340626.479	264.42	1.13	0.3934	0.95	
$18_{8,11,1}$–$17_{8,10,1}$	340659.915	264.37	1.13	0.3936	0.41	
$18_{3,16,1}$–$17_{3,15,1}$	340701.960	170.88	1.37	1.1410	0.89	
$18_{3,16,0}$–$17_{3,15,0}$	340706.208	170.88	1.37	1.1400	0.97	
$18_{7,12,0}$–$17_{7,11,0}$	340824.354	238.90	1.20	0.5285	1.32	
$18_{7,11,0}$–$17_{7,10,0}$	340824.354	238.90	1.20	0.5285	1.32	
$18_{7,11,2}$–$17_{7,10,2}$	340845.770	238.89	1.20	0.5285	0.68	
$18_{3,16,3}$–$17_{3,15,3}$	340849.327	371.42	1.38	0.1755	0.18	
$18_{7,12,1}$–$17_{7,11,1}$	340864.114	238.85	1.20	0.5287	0.62	
$18_{6,13,0}$–$17_{6,12,0}$	341145.085	216.82	1.26	0.6809	0.84	
$18_{6,12,0}$–$17_{6,11,0}$	341148.198	216.82	1.26	0.6809	0.73	
$18_{6,13,1}$–$17_{6,12,1}$	341180.939	216.77	1.26	0.6811	0.44	
$18_{6,12,2}$–$17_{6,11,2}$	341183.787	216.78	1.26	0.6810	1.54*	CH_3CHO
$18_{12,6,2}$–$17_{12,5,2}$	341334.607	399.24	1.31	0.1287	ND	
$18_{5,14,0}$–$17_{5,13,0}$	341668.402	198.18	1.31	0.8425	1.00	
$18_{5,14,1}$–$17_{5,13,1}$	341738.492	198.14	1.30	0.8341	0.96	
$18_{5,13,2}$–$17_{5,12,2}$	341745.985	198.16	1.30	0.8339	0.96	
$18_{5,13,0}$–$17_{5,12,0}$	341752.782	198.20	1.32	0.8426	0.88	
$18_{12,7,1}$–$17_{126,1}$	342038.445	398.73	1.32	0.1290	ND	
$18_{4,15,0}$–$17_{4,14,0}$	342198.102	183.00	1.36	1.0020	1.35	
$18_{4,15,1}$–$17_{4,14,1}$	342245.986	182.97	1.36	0.9980	1.35	
$18_{4,14,5}$–$17_{4,13,5}$	342379.200	384.41	1.36	0.1525	ND	
$18_{5,14,3}$–$17_{5,133}$	342515.837	397.84	1.32	0.1303	ND	
$18_{5,133}$–$17_{5,123}$	342607.846	397.85	1.32	0.1303	?*	CH_3OCH_3
$18_{3,164}$–$17_{3,154}$	342783.221	371.34	1.38	0.1742	ND	
$18_{4,15,3}$–$17_{4,14,3}$	342789.396	383.05	1.37	0.1545	ND	
$19_{11,9,1}$–$18_{11,8,1}$	352369.864	377.78	1.53	0.1822	0.68	
$19_{2,18,4}$–$18_{2,17,4}$	359228.816	378.69	1.10	0.1254	ND	
$19_{11,82}$–$18_{11,7,2}$	359247.409	378.67	1.10	0.1254	ND	
$19_{2,18,3}$–$18_{2,17,3}$	359269.912	378.63	1.10	0.1254	0.72	
$19_{11,8,0}$–$18_{11,7,0}$	359269.912	378.63	1.10	0.1254	0.72	
$19_{10,9,2}$–$18_{10,8,2}$	359312.215	342.96	1.20	0.1904	0.61	
$19_{3,17,1}$–$18_{3,16,1}$	359332.741	188.12	1.62	1.0880	1.42	
$19_{3,17,0}$–$18_{3,16,0}$	359340.064	188.13	1.62	1.0880	1.15	
$19_{10,10,1}$–$18_{10,9,1}$	359346.965	342.92	1.20	0.1904	ND	
$19_{10,10,0}$–$18_{10,9,0}$	359348.175	342.90	1.20	0.1905	ND	
$19_{10,9,0}$–$18_{10,8,0}$	359348.175	342.90	1.20	0.1905	ND	

Notes. Integrated intensities noted with a * are certainly blended with lines from other species, indicated in Col. 7 when identified.

Table A.2. continued.

Transition	Frequency (MHz)	E_{up} (K)	A_{ij} $10^{-3}(s^{-1})$	τ_{peak} 10^{-2}	$\int T_{mb}dv$ (K km s^{-1})	Blend
$19_{9,10,2}$–$18_{9,9,2}$	359433.194	310.62	1.29	0.2763	0.48	
$19_{9,11,0}$–$18_{9,10,0}$	359453.483	310.58	1.29	0.2764	0.50	
$19_{9,10,0}$–$18_{9,9,0}$	359453.483	310.58	1.29	0.2764	0.50	
$19_{3,17,3}$–$18_{3,16,3}$	359462.490	388.67	1.62	0.1674	0.43	
$19_{9,11,1}$–$18_{9,10,1}$	359473.909	310.57	1.29	0.2764	0.35	
$19_{8,12,0}$–$18_{8,11,0}$	359606.525	281.67	1.37	0.3843	0.66	
$19_{8,11,0}$–$18_{8,10,0}$	359606.525	281.67	1.37	0.3843	0.66	
$19_{8,11,2}$–$18_{8,10,2}$	359607.958	281.68	1.37	0.3842	0.40	
$19_{8,12,1}$–$18_{8,11,1}$	359642.724	281.63	1.37	0.3844	ND	
$19_{7,13,0}$–$18_{7,12,0}$	359841.586	256.17	1.44	0.5126	1.36	
$19_{7,12,0}$–$18_{7,11,0}$	359841.586	256.17	1.44	0.5126	1.36	
$19_{7,122}$–$18_{7,11,2}$	359864.837	256.16	1.44	0.5126	ND	
$19_{7,13,1}$–$18_{7,12,1}$	359883.447	256.12	1.44	0.5128	0.37	
$19_{6,14,0}$–$18_{6,13,0}$	360219.543	234.11	1.51	0.6567	0.87	
$19_{6,13,0}$–$18_{6,12,0}$	360225.285	234.11	1.51	0.6568	0.76	
$19_{6,14,1}$–$18_{6,13,1}$	360258.207	234.06	1.51	0.6570	0.67	
$19_{6,13,2}$–$18_{6,12,2}$	360262.184	234.07	1.51	0.6568	0.60	
$19_{5,15,0}$–$18_{5,14,0}$	360822.302	215.50	1.56	0.8092	1.28	
$19_{5,15,1}$–$18_{5,14,1}$	360895.231	215.46	1.53	0.7938	0.95	
$19_{5,14,2}$–$18_{5,13,2}$	360952.814	215.48	1.54	0.7939	1.33	
$19_{5,14,0}$–$18_{5,13,0}$	360959.318	215.52	1.57	0.8094	1.05	
$19_{3,17,4}$–$18_{3,16,4}$	361083.946	388.67	1.62	0.1661	ND	
$19_{4,16,0}$–$18_{4,15,0}$	361324.526	200.34	1.61	0.9583	0.91	
$19_{4,16,1}$–$18_{4,15,1}$	361359.771	200.31	1.61	0.9573	1.00	